The Fast X-Ray Transient XRT 210423 and Its Host Galaxy

D. Eappachen[1,2] , P. G. Jonker[2,1] , A. J. Levan[2], J. Quirola-Vásquez[3,4,5], M. A. P. Torres[6,7] , F. E. Bauer[3,4,8] ,
V. S. Dhillon[6,9], T. Marsh[10], S. P. Littlefair[9] , M. E. Ravasio[2] , and M. Fraser[11]

[1] SRON, Netherlands Institute for Space Research, Niels Bohrweg 4, 2333 CA, Leiden, The Netherlands; d.eappachen@sron.nl
[2] Department of Astrophysics/IMAPP, Radboud University Nijmegen, P.O. Box 9010, 6500 GL, Nijmegen, The Netherlands
[3] Instituto de Astrofísica, Pontificia Universidad Católica de Chile, Casilla 306, Santiago 22, Chile
[4] Millennium Institute of Astrophysics (MAS), Nuncio Monseñor Sótero Sanz 100, Providencia, Santiago, Chile
[5] Observatorio Astronómico de Quito, Escuela Politécnica Nacional, 170136, Quito, Ecuador
[6] Instituto de Astrofísica de Canarias, E-38205 La Laguna, S/C de Tenerife, Spain
[7] Departamento de Astrofísica, Univ. de La Laguna, E-38206 La Laguna, Tenerife, Spain
[8] Space Science Institute, 4750 Walnut Street, Suite 205, Boulder, CO 80301, USA
[9] Department of Physics & Astronomy, University of Sheffield, Sheffield S3 7RH, UK
[10] Department of Physics, Gibbet Hill Road, University of Warwick, Coventry CV4 7AL, UK
[11] School of Physics, O'Brien Centre for Science North, University College Dublin, Belfield, Dublin 4, Ireland
Received 2022 December 30; revised 2023 March 2; accepted 2023 March 2; published 2023 May 10

Abstract

Fast X-ray Transients (FXTs) are X-ray flares with durations ranging from a few hundred seconds to a few hours. Possible origins include the tidal disruption of a white dwarf by an intermediate-mass black hole, a supernova shock breakout, or a binary neutron star merger. We present the X-ray light curve and spectrum as well as deep optical imaging of the FXT XRT 210423, which has been suggested to be powered by a magnetar produced in a binary neutron star merger. Our Very Large Telescope and Gran Telescopio Canarias (GTC) observations began on 2021 May 6, thirteen days after the onset of the flare. No transient optical counterpart is found in the $1''$ (3σ) X-ray uncertainty region of the source to a depth $g_s = 27.0$ AB mag. (We use the word "counterpart" for any transient light in a wave band other than the original X-ray detection wave band, whereas the word "host" refers to the host galaxy.) A candidate host lies within the $1''$ X-ray uncertainty region with a magnitude of 25.9 ± 0.1 in the GTC/ HiPERCAM g_s filter. Due to its faintness, it was not detected in other bands, precluding a photometric redshift determination. We detect two additional candidate host galaxies: one with $z_{\mathrm{spec}} = 1.5082 \pm 0.0001$ and an offset of $4''.2 \pm 1''$ $(37 \pm 9$ kpc) from the FXT, and another one with $z_{\mathrm{phot}} = 1.04^{+0.22}_{-0.14}$ and an offset of $3''.6 \pm 1''$ $(30 \pm 8$ kpc). Based on the properties of all the prospective hosts, we favor a binary neutron star merger, as previously suggested in the literature, as the explanation for XRT 210423.

Unified Astronomy Thesaurus concepts: X-ray transient sources (1852); Tidal disruption (1696); Magnetars (992); Supernovae (1668); Dwarf galaxies (416); Globular star clusters (656)

1. Introduction

Fast X-ray transients (FXTs) have been discovered through systematic searches in Chandra, XMM-Newton, and eROSITA data by Jonker et al. (2013), Glennie et al. (2015), Irwin et al. (2016), Bauer et al. (2017), Xue et al. (2019), Alp & Larsson (2020), Novara et al. (2020), Wilms et al. (2020), Quirola-Vásquez et al. (2022), and Lin et al. (2022). FXTs manifest as short flashes of X-rays, with durations ranging from a few minutes to hours. Several different physical mechanisms have been suggested for the origin of FXTs. The leading theories explaining FXTs include events that are related to strong gravitational wave sources, such as a binary neutron star merger (BNS; Dai et al. 2006; Metzger et al. 2008) or a white dwarf (WD) disruption by an intermediate-mass black hole (IMBH; Maguire et al. 2020), as well as supernovae shock breakouts (SBOs), where those involving relatively compact progenitors are predicted to be detectable in soft X-rays (Waxman & Katz 2017).

Some neutron star mergers are thought to leave behind a rapidly rotating neutron star with a strong magnetic field (i.e., a

magnetar), which could produce an X-ray transient (Dai et al. 2006; Metzger et al. 2008; Zhang 2013; Sun et al. 2017). Xue et al. (2019) favor this scenario for XRT 150321/CDF−S XT2. The apparent plateau in its X-ray light curve, comparable to those seen in a subset of short gamma-ray bursts (SGRBs; Rowlinson et al. 2013), has been used to argue for a BNS origin.

Tidal disruption events (TDEs) involving a massive BH and a main-sequence star have timescales ranging from hours to weeks (Saxton et al. 2020). The relatively low mass of an IMBH compared to that of a supermassive black hole, coupled with the compactness of a WD compared to that of a main-sequence star, is predicted to lead to a fast X-ray flash (Rosswog et al. 2009; Maguire et al. 2020). Some of the FXTs have been interpreted as WD IMBH TDEs (e.g., XRT 000519; Jonker et al. 2013; Peng et al. 2019). Precursor flares are found in XRT 000519, and their timescales can be explained by the expected orbital timescale of a WD in an eccentric orbit around an IMBH (Jonker et al. 2013; Maguire et al. 2020).

The radiation-mediated shock from a supernova (SN) explosion crossing the star's surface releases a so-called SBO (Waxman & Katz 2017). Depending on the radius of the exploding star, the SBO could initially appear as an X-ray flash and then evolve into a UV and optical signal. The best example of an SBO is XRT 080109 (Soderberg et al. 2008) in the galaxy

NGC 2770, where the FXT was associated with a bright Type Ibc SN, SN 2008D (Mazzali et al. 2008; Modjaz et al. 2009).

About 30 FXTs have been identified to date, both serendipitously and through careful searches in archival data. Counterpart searches have been done for some FXTs. For instance, in the case of CDF-S XT1, Bauer et al. (2017) did not find a counterpart down to deep optical limits from Very Large Telescope (VLT) imaging beginning 80 minutes after the onset of the X-ray flare ($R > 25.7$ mag; Bauer et al. 2017). Consequently, deep host searches have been undertaken from both space and ground for other FXTs. For instance, deep VLT and Gran Telescopio Canarias (GTC) observations of XRT 000519 (Jonker et al. 2013) were reported by Eappachen et al. (2022). They report the detection of a candidate host galaxy to the northwest side of the FXT position in the g-band image at $m_g = 26.29 \pm 0.09$ AB mag. An SBO scenario is firmly ruled out if the FXT is indeed associated with this candidate host galaxy. If XRT 000519 is at the distance of M86, it is unlikely that an associated optical SN was missed, whereas if it is at a larger redshift, the peak X-ray luminosity would be so large it would rule out an SN SBO origin. Deep optical observations have constrained the hosts of two other FXTs: CDF-XT1 (Bauer et al. 2017) lies at a $0\rlap{.}''13$ offset from an $m_r = 27.5$ dwarf galaxy with $z_{\mathrm{phot}} = 0.4$–3.2, and CDF $-$S XT2 (Xue et al. 2019) lies at a projected distance of 3.3 ± 1.9 kpc from a $z_{\mathrm{spec}} = 0.74$ star-forming galaxy. For XRT 170901, Lin et al. (2022) find an elongated, possibly late-type, star-forming galaxy within the 2σ X-ray uncertainty region, while for XRT 030511 (Lin et al. 2022), no host galaxy was found.

In this paper, we present the X-ray light curve and spectrum of the FXT XRT 210423, our search for its optical counterpart and host galaxy, and an analysis of the potential host galaxies we identified. Throughout the paper, we use the concordance Λ-CDM cosmology, with Hubble constant $H_0 = 67.4 \pm 0.5$ km s^{-1} Mpc^{-1} and matter density parameter $\Omega_m = 0.315 \pm 0.007$ (Planck Collaboration et al. 2020). In Section 2, we describe the observations and analysis. We present the results in Section 3, which we discuss in Section 4, and we draw our conclusions in Section 5.

2. Observations and Analysis

2.1. Chandra X-Ray Data

The FXT XRT 210423 was serendipitously discovered on 2021 April 23 (Chandra Observation ID: ObsID 24604), in the direction of A1795 in Chandra archival data and reported by Lin et al. (2021). The transient position was covered by the I3 CCD of the ACIS-I array of CCD detectors. We reprocessed and analyzed the data with the CIAO 4.14 software developed by the Chandra X-Ray Center employing CALDB version 4.9.1. To identify the X-ray source as well as determine its position and its associated uncertainty, we utilize the CIAO source detection tool wavdetect (Freeman et al. 2002) using a series of "Mexican Hat" wavelet functions to account for the varying PSF size across the detector. To improve the Chandra astrometric solution, we cross-match the positions of 15 X-ray sources with those of their prospective optical counterparts that come from either the Gaia Early Data Release 3 (Gaia-EDR3; Gaia Collaboration et al. 2021) or the Sloan Digital Sky Survey Data Release 16 (SDSS–DR16; Ahumada et al. 2020) catalogs.

For this, we use the wcs_match script in CIAO. The average residual is $0\rlap{.}''82 \pm 0\rlap{.}''10$.

We extracted the source X-ray spectrum with the specextract package in CIAO. For this, we included the X-ray counts within a circular region centered at the X-ray position with a radius of $9\rlap{.}''2$ (corresponding to an encircled energy fraction of $\approx 98\%$ given its off-axis angle of $7\rlap{.}'5$; Yang et al. 2019). For the background regions, we considered two adjacent rectangular regions (centered on R.A.$_{\mathrm{J2000.0}} = 13^{\mathrm{h}}48^{\mathrm{m}}59\rlap{.}^{\mathrm{s}}27$, decl.$_{\mathrm{J2000.0}} = 26^{\{\circ\}}39\rlap{.}'33\rlap{.}''9$ and R.A.$_{\mathrm{J2000.0}} = 13^{\mathrm{h}}48^{\mathrm{m}}53\rlap{.}^{\mathrm{s}}55$, decl.$_{\mathrm{J2000.0}} = 26^{\{\circ\}}39\rlap{.}'55\rlap{.}''3$, with a size of $52\rlap{.}'' \times 17\rlap{.}''$ and a position angle of the long side of 15° with respect to the east–west axis) to cover the gradient emission of the galaxy cluster LEDA 94646, which is the main source of background photons. This procedure yields a count rate of $\approx 9.7 \times 10^{-3}$ cts s^{-1} for XRT 210423. Using the Bayesian X-ray Astronomy package (BXA; Buchner et al. 2014), within the fitting environment of XSPEC version 12.10.1f (Arnaud 1996) and Cash statistics (Cash 1979), we fitted the spectra of XRT 210423. We used an absorbed power-law model (phabs*zphabs*pow model in XSPEC) to describe the data, where phabs and zphabs describe the Galactic and intrinsic absorption, respectively. For the extraction of the X-ray spectral parameters, we fixed the Galactic hydrogen column density ($N_{H,\mathrm{Gal}}$) to 3.0×10^{20} cm^{-2} (taken from Kalberla et al. 2005; Kalberla & Haud 2015), while the intrinsic hydrogen column density (N_H) is a free parameter in our fit. In addition, we calculate the hardness ratio (see Sect. 3.1), which we define as HR $= (H\text{-}S)(H+S)^{-1}$, where H and S are the count rates in the 2.0–7.0 keV and 0.5–2.0 keV bands, respectively, and we derive their errors based on the Bayesian code BEHR (Park et al. 2006).

2.2. Optical Data

We observed the field containing the FXT XRT 210423 with the FOcal Reducer/low-dispersion Spectrograph (FORS2; Appenzeller et al. 1998) mounted on the 8.2 m Very Large Telescope (VLT) of the European Southern Observatory (ESO). FORS2 on VLT has a field of view $6\rlap{.}'8 \times 6\rlap{.}'8$ and provides a pixel scale of $0\rlap{.}''25$ with 2×2 binning. A total of 7×180 s images were taken on 2021 May 6 in the Johnson–Cousins R-band filter with the two 2×4k MIT CCDs.

The average seeing in the images was around $1\rlap{.}''8$. The ESO reflex data reduction pipeline (Freudling et al. 2013) was used for bias and flat-field correction. Next, we employed L.A. Cosmic to remove charge caused by cosmic ray hits from the images (van Dokkum 2001) and stacked them using the IRAF IMCOMBINE task. We applied an astrometric correction to the stacked image using astrometry.net[12] (Lang et al. 2010).

On 2021 May 13 and June 10, we also obtained simultaneous u_s-, g_s-, r_s-, i_s-, and z_s-band images with the HiPERCAM instrument mounted on the 10.4 m Gran Telescopio Canarias (GTC) at the Roque de los Muchachos Observatory (La Palma, Spain). Seventeen frames with exposure times of 180 s each were obtained. HiPERCAM with 2×2 binning provides a plate scale of $0\rlap{.}''16$ per pixel and a field of view of $2\rlap{.}'8 \times 1\rlap{.}'4$ on GTC (Dhillon et al. 2021). The respective average seeings in the images were around $1\rlap{.}''4$ and $0\rlap{.}''9$ for the first and second epochs.

---

[12] https://astrometry.net/

The HiPERCAM data reduction steps were performed using a dedicated data reduction pipeline, including bias subtraction, flat fielding, and fringe correction.[13] For both epochs, the 17 images were averaged to create a single deep image using the IRAF IMCOMBINE task. We scaled each image to a common level (scale = "mode") before using reject = "avsigclip" to remove charge caused by cosmic rays.

For each of the combined u_s, g_s, r_s, i_s, and z_s-band HiPERCAM images, we refined the world coordinate information that was based on the telescope pointing using the known astrometric positions of eight stars from the Pan-STARRS catalog (Chambers et al. 2016). We used the centroid algorithm in IRAF PHOT and IRAF CCMAP to determine the world coordinate solution, and we applied the astrometric corrections using IRAF CCSETWCS.

We used SExtractor (Bertin & Arnouts 1996) to extract the R.A. and decl., magnitude, and magnitude error from all the objects detected in the stacked image. Photometric calibration of the image was done using stars from the Pan-STARRS DR2 catalog data for g_s, r_s, i_s, z_s, and R filters (Chambers et al. 2016). For the zero-point value of the u_s filter, we used SDSS catalog data. For the FORS2 image, we used the transformation equation of Lupton (2005) to convert the Pan–STARRS magnitudes given in the Sloan r- and i- bands to a Johnson–Cousins R-band magnitude. The resultant GTC/HiPERCAM u_s, g_s, r_s, i_s, z_s, and the VLT/FORS2 R-filter images of the field of XRT 210423 are shown in Figure 1.

We obtained a spectrum of the galaxy SDSS J134856.75 + 263946.7, which lies $\sim 4.''2$ from the position of the FXT XRT 210423, on 2021 May 16 using the X-SHOOTER instrument mounted on the UT3 VLT (Vernet et al. 2011). X-SHOOTER is a multiwavelength (300–2500 nm), medium-resolution spectrograph mounted at the Cassegrain focus. Using slit widths of $1.''3/1.''2/1.''2$, we obtained exposures of 2×735 s, 2×680 s, and 4×300 s in the UVB, VIS, and NIR arms of the spectrograph, respectively. For data reduction, we used the ESO Reflex pipeline (Freudling et al. 2013).

3. Results

3.1. The X-Ray Light Curve and Spectrum

The Chandra X-ray position of XRT 210423 is R.A.$_{J2000.0}$ = $13^h48^m56.^s46$ and decl.$_{J2000.0}$ = $26°$ $39'44.''3$ (with a 3σ positional uncertainty of $1''$, an X-ray localization uncertainty of $0.''31$ from wavdetect, and an uncertainty of $0.''14$ associated with tying the source position to the International Celestial Reference System (ICRS), both at the 1σ confidence level; Rots & Budavári 2011). Our resulting X-ray source position is consistent with that of Lin et al. (2021). We do not detect the source in any other publicly available Chandra observation covering the field of XRT 210423. The data span a period from ≈ 13 yr before the outburst to ≈ 40 days thereafter. Indeed, Chandra revisited the XRT 210423 field ≈ 40 days after the discovery observation of XRT 210423 (ObsId 25049 DDT proposal, PI Dacheng Lin) with an exposure time of 59.3 ks. A 3σ upper limit of $F_X \lesssim 1.4 \times 10^{-15}$ erg cm^{-2} s^{-1} for the X-ray flux in the 0.5–7 keV band was obtained. Furthermore, the upper limit to any persistent flux of XRT 210423 is $F_X \lesssim 10^{-15}$ erg cm^{-2} s^{-1} in the 0.5–7 keV band at 3σ confidence level. For this upper

---

[13] https://cygnus.astro.warwick.ac.uk/phsaap/hipercam/docs/html/

limit determination, we considered all previous Chandra observations of the field, yielding a total exposure time of ~ 2 Ms (for stacking, we used the merge_obs CIAO script), and the statistic developed by Kraft et al. (1991) at 3σ confidence level.

The left panels of Figure 2 show the Chandra 0.5–7 keV light curve of XRT 210423, and its best-fit (broken power-law) model. The light curve of XRT 210423 is comprised of a net (background-subtracted) number of $116.1^{+12.4}_{-11.8}$ photons. The X-ray flash started at about 22:15:40 UT on 2021 April 23 (T_0) and lasted for ≈ 20–25 ks during a ≈ 26.4 ks Chandra observation. The time span over which 5%–95% of the total detected number of counts was registered, T_{90}, is $12.1^{+4.0}_{-4.1}$ ks. The light curve is fit well by a broken power-law model (the chi squared, the number of degrees of freedom, and the Bayesian information criterion are 17.9, 26, and −1.74, respectively), with slopes of -0.17 ± 0.06 before the break at $t_{break} = 4.3 \pm 0.4$ ks and -3.78 ± 1.22 after the break (see Figure 2). The pre-break average flux is $F_X \approx 7 \times 10^{-13}$ erg cm^{-2} s^{-1}, while a minimum flux of $F_X \approx 6$–7 $\times 10^{-14}$ erg cm^{-2} s^{-1} is measured in the last bin after the break.

The best-fitting absorbed power-law spectral model is shown in the right panel of Figure 2. The best-fit power law has an index of 2.3 ± 0.3. The spectrum has an average hardness ratio of HR = -0.2 ± 0.1. There is no evidence at the 3σ level for spectral evolution over the flare (see Figure 2, bottom left panel). In fact, fits to the spectra extracted before and after the break (dashed vertical line the left panel of Figure 2) have consistent power-law spectral indices with values of 2.4 ± 0.5 and 2.1 ± 0.7, respectively. Here, the uncertainties are given at a 90% confidence level.

3.2. Candidate Host Identification and Photometry

We do not discuss the first-epoch observation, due to the relatively lower quality of data (seeing of $\sim 1.''4$). In the second-epoch GTC observation on 2021 June 10, we detect a candidate host in the GTC/HiPERCAM g_s filter within the $\sim 1''$ circular error circle (3σ confidence) of the XRT 210423 at R.A. = $13^h48^m56.^s46$, decl. = $+26°39'44.''3$ (hereafter called cX; see the GTC/HiPERCAM g_s-filter panel in Figure 1). Using SExtractor, we obtain an aperture (15 pixels corresponding to $2.''4$ in diameter) magnitude of 25.9 ± 0.1 for this candidate host in the g_s band.

We also measured the magnitude of other possible host candidates near the XRT 210423 3σ uncertainty region. From the GTC/HiPERCAM and FORS2 images, we obtained the Kron magnitude for the candidate host that lies to the northeast (SDSS J134856.75+263946.7; hereafter called cNE) of the FXT position at R.A. and decl $13^h48^m56.^s7$, $+26°39'46.''5$. The magnitudes are $u_s = 22.89 \pm 0.15$ (the photometric uncertainty is largely dominated by zero-point uncertainty for the u_s filter), $g_s = 22.77 \pm 0.01$, $r_s = 22.76 \pm 0.02$, $i_s = 22.99 \pm 0.07$, and $z_s = 22.75 \pm 0.11$ from the GTC/HiPERCAM observations. cNE has a Kron magnitude of 22.82 ± 0.05 in the FORS2 R filter. A fainter possible host candidate to the west of the FXT (hereafter cW) that lies at R.A. = $13^h48^m56.^s2$, decl. = $+26°39'45.''1$ was detected in the u_s, g_s, r_s, i_s, z_s-band images of the GTC/HiPERCAM observation. Aperture photometry of cW for a $2.''4$ aperture diameter gives a magnitude of $u_s = 25.6 \pm 0.2$, $g_s = 25.08 \pm 0.07$, $r_s = 24.71 \pm 0.08$, $i_s = 23.9 \pm 0.1$, and $z_s = 23.4 \pm 0.1$.
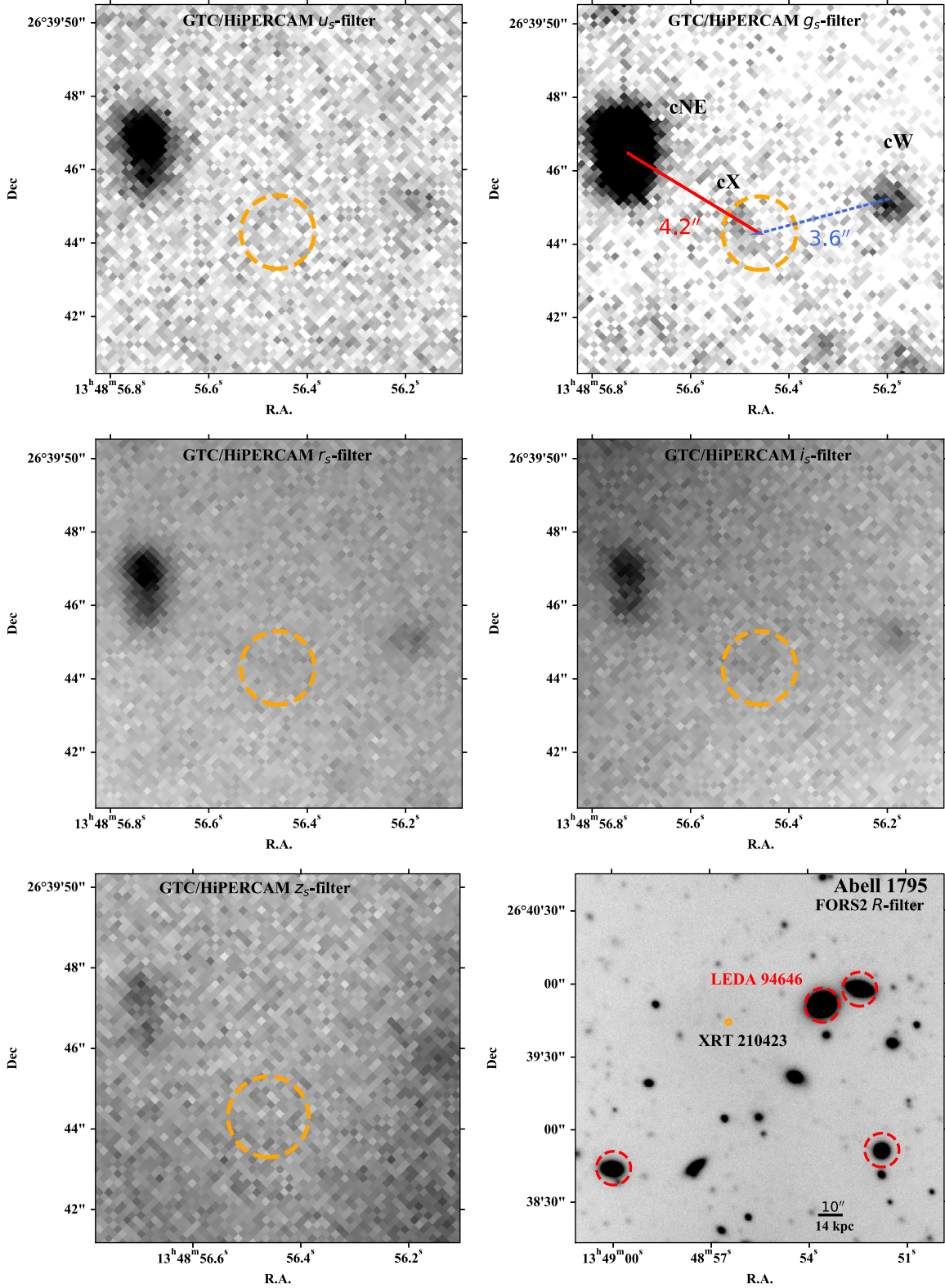
Figure 1. The second-epoch GTC/HiPERCAM, and the VLT/FORS2 images of the field of XRT 210423. From left to right and top to bottom: the GTC u_s, g_s, r_s, i_s, z_s, and the VLT R-band images. The dashed orange circle shows the FXT 3σ X-ray uncertainty position. The top right panel with the GTC/HiPERCAM g_s-filter image shows the positional offset between the center of the XRT 210423 X-ray uncertainty region and the host candidates cNE (indicated by the red line) and cW (the dashed blue line). In addition, the faint candidate host cX can (just) be seen within the 3σ FXT position. The bottom right panel shows the position of XRT 210423 with respect to the A1795 cluster in the VLT/FORS2 R filter. The FXT position is marked with an orange circle, while several members of the cluster are indicated with red dashed circles.

We determined the density of sources brighter than or as bright as the candidate host cX in the HiPERCAM g_s filter to be 0.027 objects/sq. arcsec in a region of $25'' \times 25''$ centered

on R.A. $= 13^{h}48^{m}56^{s}.5$, decl. $= +26°39'44''.8$. Assuming Poisson statistics and considering the $1''$ error region, we compute the probability of a chance alignment between XRT 210423
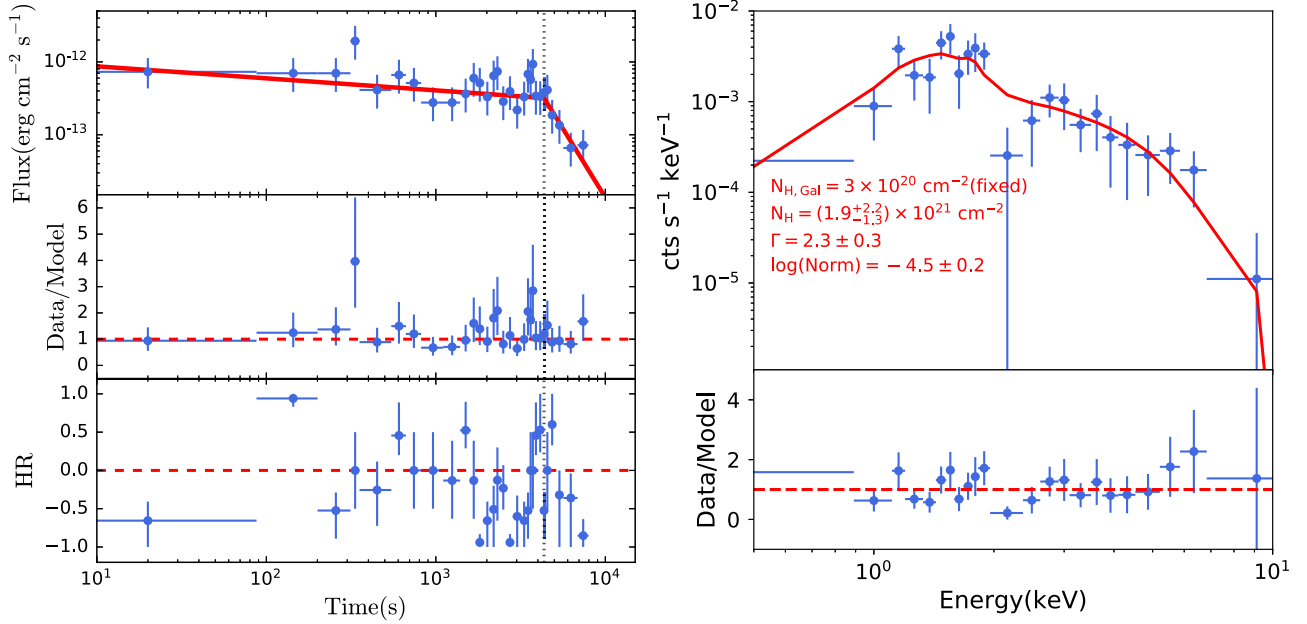
Figure 2. X-ray flux and spectral evolution of XRT 210423. Left top panel: 0.5–7 keV light curve (blue points and 1σ errors) with the best-fit broken power-law model (*red solid line*). Left middle panel: the ratio between the data and the best-fit model light curve. Left bottom panel: the hardness ratio (HR) evolution. In all three panels, the vertical dashed line ($t_B = 4350$ s) indicates the best-fit break time. We compute the light-curve zero point ($T_0 = 0$ s), dividing the light curves in bins of $\Delta t = 100$ and 10 s, and compute the chance probability that the photons per bin come from the background (P_{bkg}) using the Poisson probability and the background rate. We found that the bins after T_0 have a $P_{\mathrm{bkg}} \lesssim 0.01$, while P_{bkg} immediately before T_0 is higher, $P_{\mathrm{bkg}} \gtrsim 0.1$–0.2. Right top panel: average X-ray spectrum (blue points and 1σ errors) and the best-fit absorbed power-law model (red solid line). The text in the figure gives the parameters of the best-fit model (see main text for details). Right bottom panel: the ratio between the data and the best-fit model.

and cX to be ∼7.8%. Similarly for cNE and cW, we computed the chance alignment probability considering the $4\rlap{.}{''}2$ and $3\rlap{.}{''}6$ offset from the center of the X-ray position of XRT 210423, respectively. cNE has a chance alignment probability of ∼8.1%, whereas it is ∼16% for cW.

3.2.1. Limiting Magnitude and Completeness Limit

We did not find any transient light (counterpart) to the X-ray transient XRT 210423 in our optical observations. For the second-epoch GTC/HiPERCAM and VLT/FORS2 data, we determine the 3σ completeness and limiting magnitude using the methods explained in Eappachen et al. (2022). The completeness limits for the images taken in the corresponding filters are $u_s = 24.7$, $g_s = 25.7$, $r_s = 25.0$, $i_s = 23.9$, $z_s = 23.8$, and $R = 22.4$, whereas the limiting magnitudes are $u_s = 26.2$, $g_s = 27.0$, $r_s = 26.1$, $i_s = 24.4$, $z_s = 24.7$, and $R = 24.7$.

3.3. Spectroscopic Redshift of cNE

From the X-shooter spectrum of the galaxy cNE (SDSS J134856.75+263946.7), we determine its redshift to be 1.5082 ± 0.0001, using the faint emissions lines at $\lambda16465$ Å(rest-frame wavelength[14] $\lambda6564.6$ ÅHα), $\lambda12562$ Å(rest-frame wavelength $\lambda5008.2$ Å[O III]; the $\lambda4960.3$ Årest-wave-length emission line is not visible in the two-dimensional spectra, because the $\lambda4960.3$ Åline strength is typically a factor of 1.5 lower compared to the observed $\lambda5008.2$ Åemission line, which is just detected) and $\lambda9356$ Å(rest-frame wavelength $\lambda3729.9$ Å[O II]; $\lambda3727.1$ Åis overlapped with a sky line). The centers of the emission lines determined by eye from the two-dimensional spectra were taken for the calculation, and the

associated uncertainty is derived from the standard deviation of the redshift calculated using the three different emission lines identified. The two-dimensional spectra zoomed in on these faint emission lines are shown in the Figure 3. This redshift is consistent with that reported by Andreoni et al. (2021) and Jonker et al. (2021). The white lines seen in the two-dimensional spectra are caused by the AB nodding on slit, where the Y-axis is the spatial direction along the $11\rlap{.}{''}$ long slit.

3.4. Photometric Redshifts and Galaxy Properties

To derive the properties of galaxies cNE and cW, we employed the code BAGPIPES (Bayesian Analysis of Galaxies for Physical Inference and Parameter EStimation; Carnall et al. 2018). Using the MULTINEST sampling algorithm, BAGPIPES fits stellar population models while taking into account the star formation history and the transmission function of neutral/ionized ISM for broadband photometry and spectra. Posterior probability distributions for the host galaxy redshift (z), age, extinction by dust (A_V), star formation rate (SFR), metallicity (Z), stellar mass (M_*), and specific star formation rate (sSFR) are determined through the fit by BAGPIPES. We used an exponentially declining star formation history function and the parameterization developed by Calzetti et al. (2000) to account for dust attenuation in the spectral energy distributions (SEDs), fitting for A_V values between 0.0 and 2.0 mag as priors.

Figure 4 shows the 16th to 84th percentile range for the posterior probability distribution for the spectrum and broad-band photometry (shaded *gray* and *orange*). The input, observed, photometric data we used are shown in *blue*. We determined the photometric redshift of cW to be $z_{\mathrm{phot}} = 1.04^{+0.22}_{-0.1}$. The posterior probability distribution of the other fitted parameters are shown in the bottom panels of

---
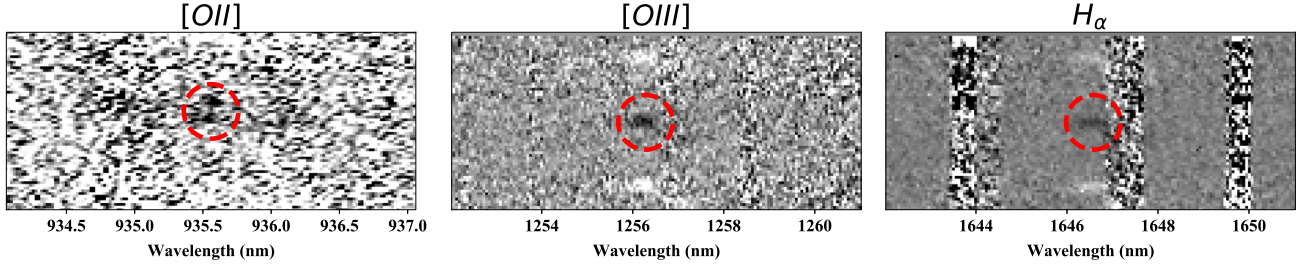[14] https://classic.sdss.org/dr6/algorithms/linestable.html

Figure 3. Three parts of the two-dimensional X-shooter spectrum of cNE (SDSS J134856.75+263946.7). We zoomed in on the faint emissions lines [O II] doublet with rest wavelengths $\lambda 3727.1$ Å and $\lambda 3729.9$ Å [O II], [O III] $\lambda 5008.2$ Å and Hα $\lambda 6564$ Å at a redshift $z = 1.5082$ marked by red dashed circles. The white horizontal lines seen in the two-dimensional spectra are caused by nodding the telescope along the slit, where the Y-axis is the spatial direction along the slit.
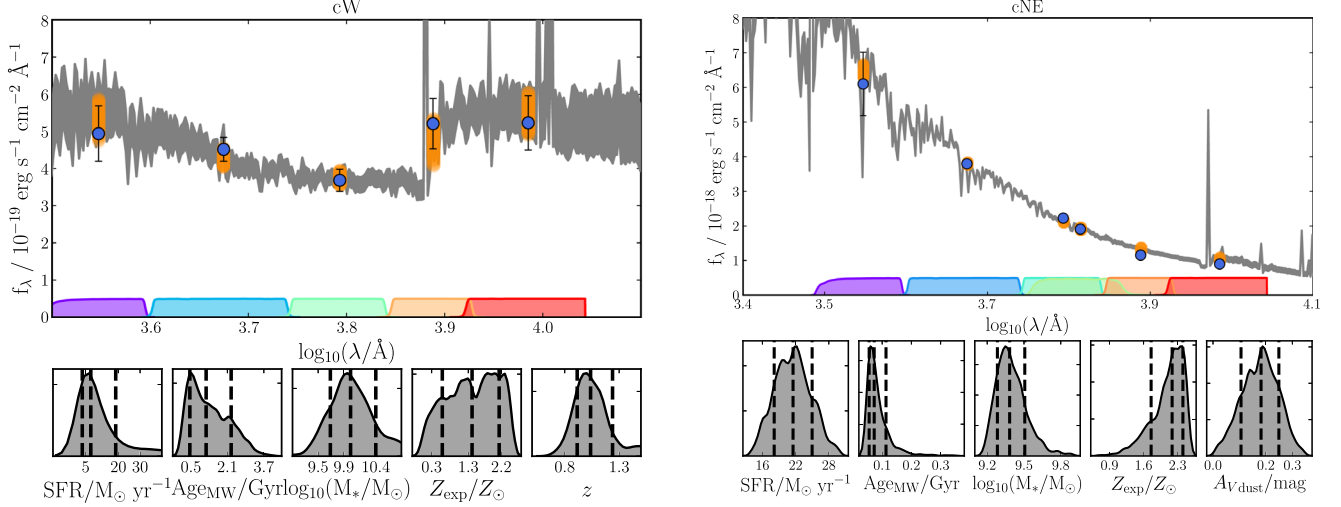
Figure 4. Best-fitting SED models obtained using the `BAGPIPES` package. The 16th–84th percentile ranges for the posterior probabilities for the spectrum and photometry (shaded gray and orange, respectively) are shown. The input, observed, photometric data and their 1σ uncertainties are given by the blue markers. The wavelength range covered by the photometric filters is marked by the colored bars at the bottom of the plot. Bottom panels: posterior probability distributions for the five fitted parameters (SFR, age, galaxy stellar mass, metallicity, and for cW only, redshift). The 16th, 50th, and 84th percentile posterior values are indicated by vertical dashed black lines. The left and right figures show the best-fitting SED models for galaxies cW and cNE, respectively.

Figure 4. Similarly, for the galaxy cNE, we obtained the posterior probability distribution for the fitted parameters, considering a fixed redshift of $z_{\rm spec} = 1.5082$ (see Section 3.2 and Figure 4).

3.5. Galaxy Offsets

We calculated the galaxy offset for the candidate host galaxies cX, cNE, and cW in the g_s-band image. The candidate host cX lies at an offset of $0''6 \pm 1''$. This corresponds to a physical offset of 0.7 ± 1.2 kpc, if the candidate host galaxy is at the distance of the A1795 cluster ($z = 0.063$). For an assumed redshift between 1 and 1.5, the physical offset ranges from 4.5 to 4.8 kpc. We computed the offset between galaxy cNE and the center of the localization uncertainty region of XRT 210423 to be $4''2 \pm 1''$. At the redshift of cNE, this angular offset translates to a physical projected offset of 37 ± 9 kpc[15]. Similarly, for galaxy cW, we derive the angular offset to be $3''6 \pm 1''$. Given the photometric redshift of 1.04 (see Section 3.3), this implies a distance of $\sim$1700 Mpc, which yields a physical offset of 30 ± 8 kpc. The offsets of the candidate host galaxies cX, cNE, and cW are shown in Figure 1.

---

[15] We use https://www.astro.ucla.edu/~wright/CosmoCalc.html

4. Discussion

In this manuscript, we report on the X-ray detection of the FXT XRT 210423. We furthermore discuss our optical observations. No optical counterpart was discovered. We do detect candidate host galaxies, and we discuss their properties and implications for the nature of this FXT. The X-ray light curve of XRT 210423 is fit well by a broken power law. The index before the break is -0.17 ± 0.06, and this part is called the plateau phase (see Figure 2). XRT 210423's light curve shares many similarities with those of several other FXTs, such as CDF−S XT2 (Xue et al. 2019), XRT 100831 (Quirola-Vásquez et al. 2022), XRT 170901 (Lin et al. 2022), XRT 030511, and XRT 110919 (Lin et al. 2022; Quirola-Vásquez et al. 2022). One of the explanations favored by Xue et al. (2019) for CDF−S XT2 is a magnetar-powered fast X-ray transient in the aftermath of the BNS merger. If true, and given the similarities in the light-curve shape, the same explanation could be used for XRT 210423. Ai & Zhang (2021) indeed suggest that the XRT 210423 data is consistent with the magnetar models of Zhang (2013), Metzger & Piro (2014), Siegel & Ciolfi (2016a, 2016b), and Sun et al. (2017). Sun et al. (2017) defines three zones where the observer would detect a different light-curve shape: if the observer's line of sight is in the jet zone, they would see a beamed SGRB signal, while if it
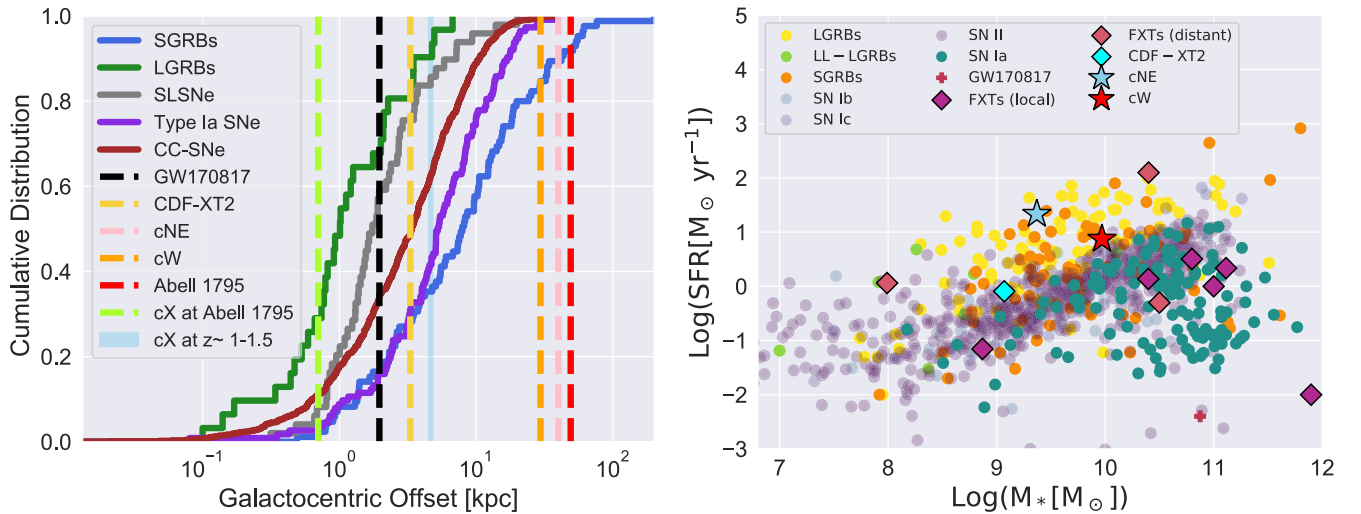
Figure 5. Left panel: projected offset of the FXT XRT 210423 with respect to the candidate host galaxies cNE (pink dashed line) and cW (orange dashed line) in comparison with the cumulative distribution of galactocentric offset in kpc seen in SGRBs (blue line; Fong et al. 2022), long gamma-ray bursts (green line; Lyman et al. 2017), superluminous supernovae (SLSNe; gray line; Schulze et al. 2021), Type Ia supernovae (violet line; Uddin et al. 2020), and core-collapse supernovae (CC-SNe; brown line; Kelly & Kirshner 2012; Schulze et al. 2021). The dashed red line indicates the projected offset of XRT 210423 with respect to the nearest galaxy LEDA 94646 of the A1795 cluster. The dashed yellow-green and light blue lines respectively show the galactocentric offset of candidate host galaxy cX if it lies at the distance of A1795 or if it has an assumed redshift between $z \sim 1$–1.5. The projected offsets for GW170817 (Levan et al. 2017) and CDF-XT2 (Xue et al. 2019) are shown with the black and yellow dashed lines. Right panel: M_* and SFR of the two candidate host galaxies cNE and cW (colored stars) compared with host galaxies of other transient events. FXT candidates reported by Quirola-Vásquez et al. (2022) and CDF-XT2 (cyan; Xue et al. 2019) are shown with diamonds. Colored circles represent LGRBs, SGRBs, low-luminosity LGRBs (see the references in Figure 13 of Quirola-Vásquez et al. 2022; Fong et al. 2022), SN Ia, SN Ib, SN Ic, and SN II (Galbany et al. 2014, Schulze et al. 2021). GW170817 is marked by the red + sign (Im et al. 2017).

is in the free zone, the observer can detect the FXT but is unlikely to detect a γ-ray burst. In the trapped zone, the X-ray emission first has to ionize the ejecta material, but when the ejecta becomes optically thin, the X-ray radiation will become detectable to an external observer. Assuming this model is true, the light curve of XRT 210423 suggests that our line of sight crosses the free zone.

The power-law decay after the break for XRT 210423 is -3.8 ± 1.2, which is consistent within 3σ with values found for other FXTs where the light curve can also be fit well with a broken power law (Xue et al. 2019; Lin et al. 2022; Quirola-Vásquez et al. 2022) . For those FXTs, the power-law index ranges between -1.6 and -2.2 (median value of -1.9 ± 0.3). The light curve decay index of XRT 210423 and similar FXTs is steeper than that of the median afterglow light-curve decay slope for GRBs (~ -1.2; Evans et al. 2009). Sun et al. (2017), in their magnetar model, suggest that the decay index might become steeper (steeper than -3) if the magnetar collapses to a black hole (Sun et al. 2017; Ai & Zhang 2021). If the magnetar does not collapse to a black hole, the X-ray light curve in the free zone would follow a decay with a power-law index between -1 and -2 (Sun et al. 2017).

A host association and a host redshift determination would help determine the (peak) luminosity and energy associated with the transient and will allow to convert an angular to a physical offset. Constraints on any or all of these parameters will help constrain the FXT nature. Therefore, we discuss in detail the implications for each of the three possible host galaxies for XRT 210423.

4.1. Assuming cX Is the Host Galaxy for XRT 210423

In our second-epoch GTC/HiPERCAM observations, we detect the candidate host galaxy cX with the $g_s = 25.9 \pm 0.1$ within the $\sim 1''$ X-ray uncertainty region (see Section 3.2). The

lack of detections at other photometric bands precludes the determination of the photometric redshift. If it is at the distance of the A1795 cluster ($z = 0.063$), then cX lies at a (projected) offset of 0.7 ± 1.2 kpc from the FXT. Alternatively, if cX is at the distance of galaxy cNE or cW, the (projected) offset would be 4.8 ± 8.7 kpc or 4.5 ± 8.2 kpc, respectively. The *left* panel of Figure 5 shows the cumulative host galaxy offset distribution of SGRBs (Fong et al. 2022), long GRBs (Lyman et al. 2017), superluminous supernovae (Schulze et al. 2021), Type Ia SNe (Uddin et al. 2020), and core-collapsed SNe (CC-SNe; Kelly & Kirshner 2012; Schulze et al. 2021), compared with the offsets (in kpc) of GW170817 (Levan et al. 2017), CDF−S XT2 (Xue et al. 2019), and XRT 210423. The possible offsets between XRT 210423 and cX are similar to the offsets seen for CDF−S XT2, SGRBs, LGRBs, SLSNe, and Type Ia SNe (see left panel of Figure 5).

If cX is at the distance of the Abell cluster, it has an absolute magnitude of $M_g = -11.4$. Given this absolute magnitude and the fact that cX seems to be an extended source, we can rule out a globular cluster host, considering the observed absolute magnitudes and sizes of globular clusters (Simon 2019). We cannot rule out the possibility that the candidate host galaxy is a faint dwarf galaxy at the distance of the Abell cluster. If so, then the X-ray flare could be due to an IMBH-WD TDE (Maguire et al. 2020). If cX lies at the distance of cNE or cW, the candidate host galaxy would have an absolute magnitude of -19.3 or -18.2, respectively. We cannot discard a dwarf galaxy association even if at such a redshift, as these absolute magnitudes are similar to that of the Large Magellanic Cloud (Belokurov & Evans 2022).

4.2. Assuming cNE Is the Host Galaxy for XRT 210423

If XRT 210423 is associated with the candidate host galaxy cNE, which has a luminosity distance of ~ 11 Gpc, the transient
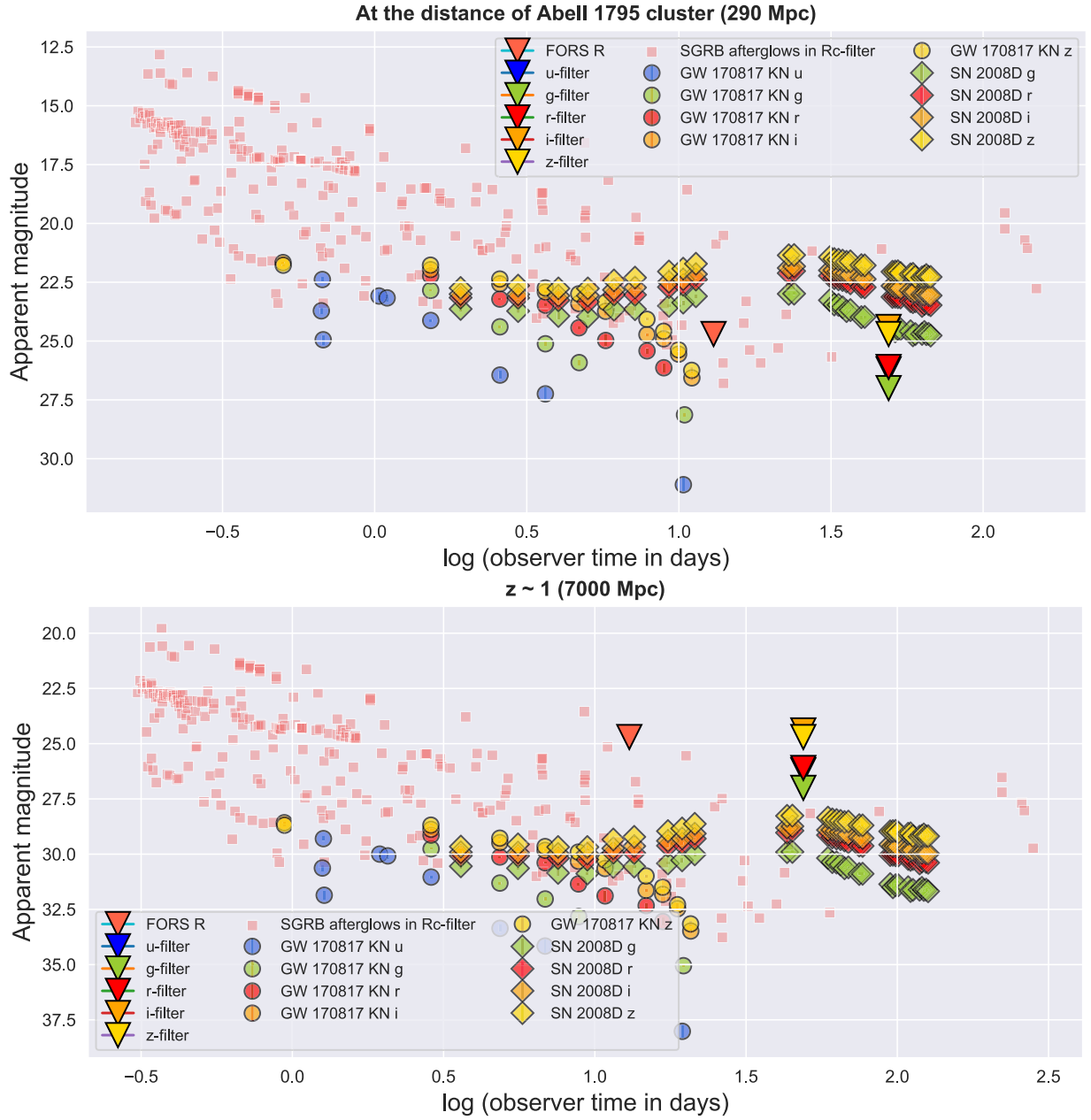
Figure 6. We compare our deep optical limits (shown with colored triangles; the symbol for the *u* filter falls behind that of the *r* filter and is thus not visible) derived from the follow-up observations of XRT 210423 using VLT/FORS2 and GTC/HiPERCAM data 13 and 55 days after the event, respectively, with the light curve of the kilonova associated with GW170817 observed in different filters (GW170817 KN; Cowperthwaite et al. 2017) as shown with differently colored circles. The different filter light curves of the supernova associated with the SBO, SN 2008D (Soderberg et al. 2008), are shown using diamond symbols. Again, observations in different filters are marked using different colors. We plotted both light curves for two distances, where in the top panel we assume the distance of A1795, and in the bottom panel we assume the distance associated with a redshift, $z = 1$. Considering the supernova signal following an SN SBO, such as SN 2008D, it is unlikely that we did not detect a counterpart if XRT 210423 occurred at the distance of the A1795 cluster. Our VLT/FORS R-filter observation is deeper than the apparent magnitude the supernova SN 2008D would have had if it occurred at the distance of the A1795 cluster. However, in order to detect a kilonova such as that in GW170817, we need lower-latency and deeper observations if a kilonova is associated with the FXT XRT 210423. To detect either an SBO or kilonova at the $z \sim 1$, we need deeper and more prompt observations within 10 days.

would have a peak X-ray luminosity of $\sim 10^{46}$ erg s^{-1}. This is consistent with the suggestion of Berger (2014) that BNS mergers have an X-ray peak luminosity of $L_{X,peak} \approx 10^{44}$–$10^{51}$ erg s^{-1} (considering beamed emission for larger luminosity). The XRT 210423 luminosity at this distance is also consistent with the luminosity of CDF−S XT2 for which a distance has been determined through a host galaxy association (Xue et al. 2019). The offset of XRT 210423 with respect to the candidate host galaxy cNE is consistent with the 90th percentile of the SGRB offsets. The parameters, such as SFR and stellar

mass of cNE, obtained through the SED fitting using BAGPIPES are shown in Figure 5. In the *right panel* of Figure 5, we show the stellar mass (M_*) and star formation rate (SFR) of the candidate host galaxy cNE (colored star) compared with host galaxies of other transient events. The FXT sample within 100 Mpc (Quirola-Vásquez et al. 2022) tends to have more massive hosts and lower SFR rates than more distant FXTs. The values for XRT 041230, XRT 080819, and XRT 141001 for the sample of FXTs with distances larger than 100 Mpc have a larger spread than those for the sample of

FXTs within 100 Mpc. cNE has a high SFR compared to the candidate hosts of most FXTs.

The star formation rate and the mass of cNE are consistent with some of the hosts of SGRBs and LGRBs (orange circles and yellow circles, respectively, in the *right panel* of Figure 5). An SBO origin of the XRT 210423 is very unlikely, given the low probability to have such a high peak luminosity ($L_{\rm X,peak} \lesssim 10^{45}$ erg s^{-1} for supernova SBOs; Soderberg et al. 2008; Waxman & Katz 2017; Goldberg et al. 2022), offset (see Figure 5; Kelly & Kirshner 2012; Uddin et al. 2020; Schulze et al. 2021), M_*, and SFR (see Figure 5; Galbany et al. 2014).

4.3. Assuming cW Is the Host Galaxy

The photometric redshift of cW $z_{\rm phot} \approx 1.04^{+0.22}_{-0.14}$. If XRT 210423 lies at the distance of cW, it had a peak luminosity of $(3-7) \times 10^{45}$ erg s^{-1} and a projected physical offset of 30 ± 8 kpc (pink line in the left panel of Figure 5). A few SGRBs (orange circles in the right panel of Figure 5) originate from hosts with similar SFR and M_* (cW has an SFR ~ 7.5 $M_\odot$ yr^{-1} and M_* [$M_\odot$] $\sim 10^{10}$; right panel of Figure 5). As in the case of cNE, the host galaxy SFR and $M_\star$, the offset between the center of the host and the FXT uncertainty region, and the peak X-ray luminosity agree with the values found for SGRBs, making a BNS merger scenario possible for XRT 210423. We discard an SBO origin for XRT 210423 based on the high X-ray luminosity and the large physical offset.

4.4. Assuming XRT 210423 Is Associated with A1795

We already briefly discussed a possible association of XRT 210423 with the galaxy cluster A1795 in Section 4.1. However, even if XRT 210423 is not associated with cX, it could be associated with A1795, which is at $z = 0.063$ (~ 290 Mpc). This is what we discuss here. If XRT 210423 originated at the distance of the A1795 cluster, the projected separation to the closest cataloged cluster galaxy, LEDA 94646 (R.A.:$13^{\rm h}48^{\rm m}53^{\rm s}6$, decl.: $+26°39'52''$), is ~ 49.1 kpc (bottom right panel of Figure 1). Although this large of an offset is rare, it is not impossible for an SGRB host. On the other hand, the associated offset is too large for a core-collapse SN or a type Ia SN origin of XRT 210423. For the distance of 290 Mpc, XRT 210423 had a peak luminosity of 7×10^{42} erg s^{-1}. We cannot rule out any of the progenitor models we consider here, given the peak X-ray luminosity. However, if associated with a typical type Ia supernova (peak absolute magnitude of -19 in the V band; Hillebrandt & Niemeyer 2000) or a CC-SNe (peak absolute magnitude of -17.5 in the B band; Richardson et al. 2014) at the distance of the cluster, the optical supernova would have a peak magnitude of $m_V \sim 18.5$ or $m_B \sim 20$, respectively. Therefore, it is unlikely that the associated optical supernova went undetected in our deep observations (see Figure 6).

5. Conclusion

We present the X-ray light curve and spectrum and the search for a possible host galaxy of the FXT XRT 210423. We consider various candidate hosts for XRT 210423: a candidate host galaxy, called cX, detected in the g_s-filter of the GTC/HiPERCAM image with a magnitude of 25.9 ± 0.1 that falls within the 3σ X-ray uncertainty region; a candidate host at a redshift $z_{\rm spec} \approx 1.51$, named cNE; and a candidate host at a redshift $z_{\rm phot} \approx 1.04$, named cW. Finally, we also investigate if XRT 210423 can be associated with the galaxy cluster A1795. Considering the association of XRT 210423 with the candidate host cX in the 3σ X-ray uncertainty region, both a BNS and a WD-IMBH TDE origin remain plausible. For all host scenarios, we can rule out the possibility that the FXT originates in an SN SBO. The galactocentric offset, star formation rate, mass, and luminosity of the candidate hosts cW and cNE are consistent with a BNS merger origin. The plateau in the X-ray light curve is similar to that of the FXT CDF $-$S XT2, also seen in some SGRBs, consistent with a BNS merger origin.

ORCID iDs

D. Eappachen ⊙ https://orcid.org/0000-0001-7841-0294
P. G. Jonker ⊙ https://orcid.org/0000-0001-5679-0695
J. Quirola-Vásquez ⊙ https://orcid.org/0000-0001-8602-4641
M. A. P. Torres ⊙ https://orcid.org/0000-0002-5297-2683
F. E. Bauer ⊙ https://orcid.org/0000-0002-8686-8737
S. P. Littlefair ⊙ https://orcid.org/0000-0001-7221-855X
M. E. Ravasio ⊙ https://orcid.org/0000-0003-3193-4714
M. Fraser ⊙ https://orcid.org/0000-0003-2191-1674

References

Ahumada, R., Allende Prieto, C., Almeida, A., et al. 2020, ApJS, 249, 3
Ai, S., & Zhang, B. 2021, ApJL, 915, L11
Alp, D., & Larsson, J. 2020, ApJ, 896, 39
Andreoni, I., Perley, D., Kasliwal, M., et al. 2021, ATel, 14641, 1
Appenzeller, I., Fricke, K., Fürtig, W., et al. 1998, Msngr, 94, 1
Arnaud, K. A. 1996, in ASP Conf. Ser. 101, XSPEC: The First Ten Years, ed. G. H. Jacoby & J. Barnes (San Francisco, CA: ASP), 17
Bauer, F. E., Treister, E., Schawinski, K., et al. 2017, MNRAS, 467, 4841
Belokurov, V., & Evans, N. W. 2022, NatAs, 6, 911
Berger, E. 2014, ARA&A, 52, 43
Bertin, E., & Arnouts, S. 1996, A&AS, 117, 393
Buchner, J., Georgakakis, A., Nandra, K., et al. 2014, A&A, 564, A125
Calzetti, D., Armus, L., Bohlin, R. C., et al. 2000, ApJ, 533, 682
Carnall, A. C., McLure, R. J., Dunlop, J. S., & Davé, R. 2018, MNRAS, 480, 4379
Cash, W. 1979, ApJ, 228, 939
Chambers, K. C., Magnier, E. A., Metcalfe, N., et al. 2016, arXiv:1612.05560
Cowperthwaite, P. S., Berger, E., Villar, V. A., et al. 2017, ApJL, 848, L17
Dai, Z. G., Wang, X. Y., Wu, X. F., & Zhang, B. 2006, Sci, 311, 1127
Dhillon, V. S., Bezawada, N., Black, M., et al. 2021, MNRAS, 507, 350

Eappachen, D., Jonker, P. G., Fraser, M., et al. 2022, MNRAS, 514, 302
Evans, P. A., Beardmore, A. P., Page, K. L., et al. 2009, MNRAS, 397, 1177
Fong, W.-f., Nugent, A. E., Dong, Y., et al. 2022, ApJ, 940, 56
Freeman, P. E., Kashyap, V., Rosner, R., & Lamb, D. Q. 2002, ApJS, 138, 185
Freudling, W., Romaniello, M., Bramich, D. M., et al. 2013, A&A, 559, A96
Gaia Collaboration, Brown, A. G. A., Vallenari, A., et al. 2021, A&A, 649, A1
Galbany, L., Stanishev, V., Mourão, A. M., et al. 2014, A&A, 572, A38
Glennie, A., Jonker, P. G., Fender, R. P., Nagayama, T., & Pretorius, M. L. 2015, MNRAS, 450, 3765
Goldberg, J. A., Jiang, Y.-F., & Bildsten, L. 2022, ApJ, 933, 164
Hillebrandt, W., & Niemeyer, J. C. 2000, ARA&A, 38, 191
Im, M., Yoon, Y., Lee, S.-K. J., et al. 2017, ApJL, 849, L16
Irwin, J. A., Maksym, W. P., Sivakoff, G. R., et al. 2016, Natur, 538, 356
Jonker, P., Levan, A., Torres, M., Eappachen, D., & Quirola, J. 2021, TNSAN, 160, 1
Jonker, P. G., Glennie, A., Heida, M., et al. 2013, ApJ, 779, 14
Kalberla, P. M. W., Burton, W. B., Hartmann, D., et al. 2005, A&A, 440, 775
Kalberla, P. M. W., & Haud, U. 2015, A&A, 578, A78
Kelly, P. L., & Kirshner, R. P. 2012, ApJ, 759, 107
Kraft, R. P., Burrows, D. N., & Nousek, J. A. 1991, ApJ, 374, 344
Lang, D., Hogg, D. W., Mierle, K., Blanton, M., & Roweis, S. 2010, AJ, 139, 1782
Levan, A. J., Lyman, J. D., Tanvir, N. R., et al. 2017, ApJL, 848, L28
Lin, D., Irwin, J. A., & Berger, E. 2021, ATel, 14599, 1
Lin, D., Irwin, J. A., Berger, E., & Nguyen, R. 2022, ApJ, 927, 211
Lupton, R. 2005, Lupton transformation equations, https://classic.sdss.org/dr4/algorithms/sdssUBVRITransform.html
Lyman, J. D., Levan, A. J., Tanvir, N. R., et al. 2017, MNRAS, 467, 1795
Maguire, K., Eracleous, M., Jonker, P. G., MacLeod, M., & Rosswog, S. 2020, SSRv, 216, 39
Mazzali, P. A., Valenti, S., Della Valle, M., et al. 2008, Sci, 321, 1185
Metzger, B. D., & Piro, A. L. 2014, MNRAS, 439, 3916
Metzger, B. D., Quataert, E., & Thompson, T. A. 2008, MNRAS, 385, 1455
Modjaz, M., Li, W., Butler, N., et al. 2009, ApJ, 702, 226
Novara, G., Esposito, P., Tiengo, A., et al. 2020, ApJ, 898, 37
Park, T., Kashyap, V. L., Siemiginowska, A., et al. 2006, ApJ, 652, 610
Peng, Z.-K., Yang, Y.-S., Shen, R.-F., et al. 2019, ApJL, 884, L34
Planck Collaboration, Aghanim, N., Akrami, Y., et al. 2020, A&A, 641, A6
Quirola-Vásquez, J., Bauer, F. E., Jonker, P. G., et al. 2022, A&A, 663, A168
Richardson, D., Jenkins, Robert, L., Wright, I., & Maddox, L, J. 2014, AJ, 147, 118
Rosswog, S., Ramirez-Ruiz, E., & Hix, W. R. 2009, ApJ, 695, 404
Rots, A. H., & Budavári, T. 2011, ApJS, 192, 8
Rowlinson, A., O'Brien, P. T., Metzger, B. D., Tanvir, N. R., & Levan, A. J. 2013, MNRAS, 430, 1061
Saxton, R., Komossa, S., Auchettl, K., & Jonker, P. G. 2020, SSRv, 216, 85
Schulze, S., Yaron, O., Sollerman, J., et al. 2021, ApJS, 255, 29
Siegel, D. M., & Ciolfi, R. 2016a, ApJ, 819, 14
Siegel, D. M., & Ciolfi, R. 2016b, ApJ, 819, 15
Simon, J. D. 2019, ARA&A, 57, 375
Soderberg, A. M., Berger, E., Page, K. L., et al. 2008, Natur, 453, 469
Sun, H., Zhang, B., & Gao, H. 2017, ApJ, 835, 7
Uddin, S. A., Burns, C. R., Phillips, M. M., et al. 2020, ApJ, 901, 143
van Dokkum, P. G. 2001, PASP, 113, 1420
Vernet, J., Dekker, H., D'Odorico, S., et al. 2011, A&A, 536, A105
Waxman, E., & Katz, B. 2017, in Handbook of Supernovae, ed. A. Alsabti & P. Murdin (Cham: Springer), 967
Wilms, J., Kreykenbohm, I., Weber, P., et al. 2020, ATel, 13416, 1
Xue, Y. Q., Zheng, X. C., Li, Y., et al. 2019, Natur, 568, 198
Yang, G., Brandt, W. N., Zhu, S. F., et al. 2019, MNRAS, 487, 4721
Zhang, B. 2013, ApJL, 763, L22